

## Computations of $SV$ Waves in Realistic Earth Models\*

R. Kind and G. Müller

Geophysical Institute, University of Karlsruhe

Received October 14, 1974

*Abstract.* The reflectivity method for the calculation of theoretical body-wave seismograms is extended to include a double-couple point source. Theoretical seismograms of  $SV$  waves from this type of source are presented for models of the earth's crust and the crust-mantle boundary, and for models of the whole earth. In the models of the crust-mantle boundary, there are up to four  $SV$  head waves, depending on the sharpness of the transition. The most remarkable one is slightly slower and later than  $S_n$  and has unusually low frequencies. Theoretical  $SV$ -wave seismograms for models of the whole earth for periods from 15 s to 60 s and in the epicentral distance range from  $10^\circ$  to  $160^\circ$  show as prominent phases  $S$ ,  $S_cS$ ,  $SKS$  and  $SKKS$ .  $SKS$  and  $SKKS$  are different in wave form, in agreement with observations from long-period  $WWNSS$  stations. A diffracted wave  $SP_{\text{diff}}KS + SKP_{\text{diff}}S$  is found in the theoretical seismograms whose travel-time curve is tangential to that of  $SKS$  at a distance of  $107^\circ$ . The resulting interference causes the wave form of  $SKS$  to change markedly around  $120^\circ$ . Since the theoretical seismograms are the complete response of the earth models from the crust-mantle boundary down to the inner core, they also include many multiple and converted phases. Besides those associated with the crust-mantle boundary there are phases related to the transition zones in the upper mantle. Their amplitudes depend strongly on the sharpness of these zones.

*Key words:* Theoretical Seismograms — Wave Theory — Earth Structure.

### Introduction

The interest of seismologists in seismic body waves seems to have increased during the last years not only due to the new possibilities that are offered by arrays but also because methods are now available to investigate, with conventional stations, the *dynamic* properties of these waves. Seismologists have always expressed the view that these properties, i. e. amplitude and wave form, contain information about the wave velocities and density within the earth which supplements and in some important cases *exceeds* the information from the kinematic properties, i. e. travel times and ray parameters. Only recently, however, methods for body wave computations in earth models with arbitrary depth dependence of velocities and density have been developed to the stage of allowing their more or less routine application to observations. High quality data, i. e. records from well-calibrated, identical stations with sufficiently close spacing, are a basic condition for quantitative interpretations. They are now routinely obtained in explosion seismological experiments like that described by Hirn *et al.* (1973) and Kind (1974). In earthquake seismology, such data are available since about 10 years from the Worldwide Network of Standardized Seismographs (WWNSS) and from the Canadian Seismic Network (CSN).

---

\* Contribution No. 117, Geophysical Institute, University of Karlsruhe.

We consider the *long-period* records from the approximately 150 stations of these two networks as an especially abundant source of information about the elastic and also anelastic properties of the earth. Up to now, only a few quantitative interpretations of long-period data have been published. Examples are papers by Mitchell and Helmberger (1973) on the *SH* components of *S* and *S<sub>c</sub>S*, by Müller (1973a) on *PKP*, and by Helmberger and Engen (1974) on the *SH* component of *S* travelling through the upper mantle. Our present work is mainly directed towards an investigation of the core-mantle boundary using the *SV* component of *S<sub>c</sub>S* together with *SKS* and *SKKS*. Our calculations of theoretical *SV*-wave seismograms for both simple and realistic models gave a number of interesting results which are compiled in this paper. Data analysis and interpretation in terms of earth structure are under way and will be published separately.

Two different methods are presently being used for the calculation of theoretical seismograms for point sources in vertically inhomogeneous half spaces or spheres, generalized ray theory and the reflectivity method. By now, generalized ray theory is relatively well known and used by various authors. The same is not yet true for the reflectivity method which was introduced by Fuchs (1968b) and developed further by Fuchs and Müller (1971). However, this method deserves wider distribution since it is more exact than generalized ray theory in that it includes *all* wave types in the reflecting medium—primary reflections, multiple reflections and converted waves. By contrast, when using generalized ray theory one normally has to restrict the calculation to primary reflections. Multiples and conversions can be included only in special cases. For instance, it would be quite hard to calculate theoretical seismograms for *SKKS* or *SKKKS* with generalized ray theory whereas these phases are automatically included in computations with the reflectivity method, as can be seen later in this paper.

Both generalized ray theory and the reflectivity method are methods for layered half spaces. In computations for spherical earth models, an earth flattening approximation (EFA) is usually applied beforehand. There are derivations of the EFA from a comparison of both geometric ray theory (Müller, 1971, 1973b) and wave theory (Hill, 1972; Chapman, 1973) for a sphere and a half space. Both approaches give almost the same results for the transformation of the sphere into a half space, but it seems that the simple approach, based on geometric ray theory, gives a more complete EFA since it also includes the possibility that the point source and the receiver are at different depths. The range of applicability of the EFA has been discussed by Müller (1973b) with the aid of a numerical experiment and found to include waves with periods of up to 30 s, propagating as deep as several hundred kilometers below the boundary of the inner core. The similarity of observed and theoretical seismograms for core phases in Müller (1973a) is in itself a qualitative proof that the EFA has a wide range of applications. Buchbinder (1974) recently noted this similarity in the case of the diffraction at the caustic of *PKIP* which produces a very low frequent and dispersed precursor to *PKIKP* in long-period records. Another example is given in Fig. 18 of the present paper for *SKS* and *SKKS*. In this case, the theoretical seismogram shows the same difference in pulse form between the two phases as the observed records.

The following section gives a brief account of the reflectivity method for a double-couple point source in a layered half space. The introduction of this source type is

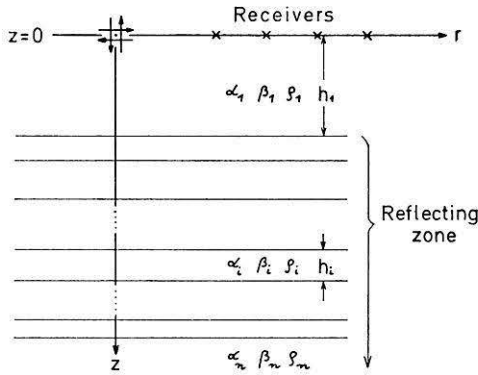


Fig. 1. Double-couple point source with special orientation in a layered medium

necessary, since the final aim of our work is the investigation of waves from earthquakes. Details of the derivation and formulas are given in the appendices A and B. First examples of theoretical  $SV$ -wave seismograms for two half spaces, separated by a first-order discontinuity or a transition zone, are then discussed. The system of head waves in these models is particularly interesting from a theoretical point of view. A seismogram section is also given for a realistic model of the earth's crust, derived from recent refraction experiments. The main part of this paper gives results for the propagation of  $SV$  waves in different models of the whole earth. One  $P$ -wave seismogram section is also included. The  $SV$  sections show, besides the main body-wave phases  $S$ ,  $S_cS$ ,  $SKS$  and  $SKKS$ , a surprising number of additional, mostly weaker, phases. Most of them are multiples and converted wave types which are produced at discontinuities and transition zones of the models; one is a wave, diffracted at the earth's core and related to  $SKS$ . The identification of these phases was mainly made with the aid of their travel times. The investigation of these minor phases is necessary for our work on the main  $SV$  phases, since there may be interference. Some of these phases may also be of interest in the study of the fine structure of the earth's mantle.

*Basic Formulas*

Fig. 1. shows the geometry of the double-couple point source and the layered medium that is assumed in all calculations of this paper. This is a special and simple case of the more general geometry treated in Appendix A. The model consists of a reflecting zone below a homogeneous half space. The half space contains source and receivers and is characterized by the  $P$  velocity  $\alpha_1$ , the  $S$  velocity  $\beta_1$  and the density  $\rho_1$ . The distance of source and receivers from the reflecting zone is  $h_1$ . The reflecting zone consists of  $n-2$  layers and a half space;  $n$  is the total number of different media. The force system of the double couple is located in a vertical plane, and the receivers are assumed to lie in this plane along a horizontal profile through the source. As Fig. 2 shows, the  $SV$  radiation of the double couple is maximum along the  $z$ -axis whereas the  $P$  radiation vanishes in this direction. There is no  $SH$  motion at the receivers, and  $SV$  and  $P$  waves are polarized in the vertical plane through the receivers.

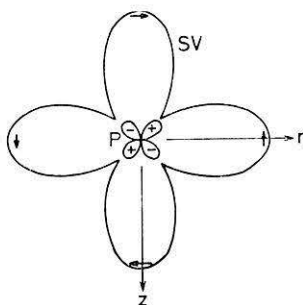


Fig. 2. Far-field radiation characteristics of the double couple in the vertical plane, containing the receivers. The *SV* motion is transversal, the *P* motion longitudinal. It has been assumed that the velocity ratio  $\alpha_1/\beta_1$  is  $|\sqrt{3}$

This is true for both the direct waves and the reflections from the reflecting zone. The usual description of the time dependence of a double couple is by the moment function  $M(t)$ . In the far field, all displacements of the direct waves have the form of the derivative  $M'(t)$ .

If  $\bar{M}(\omega)$  ( $\omega =$  circular frequency) is the Fourier transform of  $M(t)$ , then the Fourier transform of the horizontal and vertical displacements of the reflected *SV* wave at the receivers, due to the incident *SV* wave, are (see Appendix A):

$$\bar{u}_r = -\frac{\omega^2 \bar{M}(\omega)}{4\pi \rho_1 \beta_1^4} \int_{\gamma_1}^{\gamma_2} (2 \sin^2 \gamma - 1) \sin \gamma \cos \gamma R_{ss}(\omega, \gamma) J_0 \left( \frac{\omega r}{\beta_1} \sin \gamma \right) \exp \left( -i \frac{2b_1 \omega}{\beta_1} \cos \gamma \right) d\gamma \quad (1)$$

$$\bar{u}_z = \frac{i\omega^2 \bar{M}(\omega)}{4\pi \rho_1 \beta_1^4} \int_{\gamma_1}^{\gamma_2} (2 \sin^2 \gamma - 1) \sin^2 \gamma R_{ss}(\omega, \gamma) J_1 \left( \frac{\omega r}{\beta_1} \sin \gamma \right) \exp \left( -i \frac{2b_1 \omega}{\beta_1} \cos \gamma \right) d\gamma \quad (2)$$

In the following, these displacements are called the *SS* response of the medium. Analogously, the *PP* response is:

$$\bar{u}_r = -\frac{\omega^2 \bar{M}(\omega)}{2\pi \rho_1 \alpha_1^4} \int_{\gamma_1}^{\gamma_2} \sin^3 \gamma \cos \gamma R_{pp}(\omega, \gamma) J_0 \left( \frac{\omega r}{\alpha_1} \sin \gamma \right) \exp \left( -i \frac{2b_1 \omega}{\alpha_1} \cos \gamma \right) d\gamma \quad (3)$$

$$\bar{u}_z = -\frac{i\omega^2 \bar{M}(\omega)}{2\pi \rho_1 \alpha_1^4} \int_{\gamma_1}^{\gamma_2} \sin^2 \gamma \cos^2 \gamma R_{pp}(\omega, \gamma) J_1 \left( \frac{\omega r}{\alpha_1} \sin \gamma \right) \exp \left( -i \frac{2b_1 \omega}{\alpha_1} \cos \gamma \right) d\gamma \quad (4)$$

In these expressions,  $i$  is the imaginary unit,  $\gamma$  is the real angle of incidence at the top of the reflecting zone,  $\gamma_1$  and  $\gamma_2$  are the limits of  $\gamma$  and are chosen according to the waves of interest.  $R_{ss}(\omega, \gamma)$  and  $R_{pp}(\omega, \gamma)$  are the plane-wave reflection coefficients (or reflectivities) of the reflecting zone which normally depend both on  $\omega$  and  $\gamma$ . Some explanations, concerning the calculation of  $R_{ss}(\omega, \gamma)$ , are given in Appendix B.  $J_0$  and  $J_1$  are Bessel functions of the first kind. Details of the calculation of theoretical seismograms with the aid of formulas such as (1) through (4) have been given by Fuchs and Müller (1971).

For the calculations of this paper, the following assumption has been made about the spectrum of the double-couple moment function:

$$\bar{M}(\omega) = \frac{1}{2} \left( 1 + \cos \frac{\pi\omega}{\omega_0} \right), \quad -\omega_0 \leq \omega \leq \omega_0$$

$\omega_0$  is the (circular) cutoff frequency.  $M'(t)$ , the derivative of the moment function, is approximately one sine period with duration  $T \approx 15/\omega_0$ . This pulse, and therefore also the direct wave from the double couple, are acausal, i.e., they are nonzero for negative times. The essential acausality can be removed by a shift to greater times by  $T/2$ . This time shift is applied to all theoretical seismograms.

#### *Theoretical Seismograms for SV Waves in Crustal Models*

In this section, theoretical seismograms for a few models of the earth's crust will be presented.

Figs. 3 and 4 show plots of the horizontal displacement component of the  $SS$  response of a 30 km thick homogeneous crust, overlying a homogeneous mantle. The crust-mantle boundary (Moho) is a first-order discontinuity. The free surface is not included in the model, neither at the source nor at the receiver. The main frequency of the input signal is 7 Hz. The main phase in Fig. 3 is the reflection from the Moho. The same seismograms as in Fig. 3 are plotted in Fig. 4 on a ten times larger amplitude scale. Now, three weak head waves are visible in addition to the Moho reflection, one with the  $P$  velocity of the mantle, one with the  $P$  velocity of the crust, and one with the  $S$  velocity of the mantle, the last type-being the  $S_n$  wave of our model. The head wave  $S_1P_2S_1$  originates from  $S$ - $P$  and  $P$ - $S$  conversions at the Moho and is expected to exist. A head wave of the type  $S_1P_1S_1$ , travelling with the  $P$  velocity of the crust, is less familiar although not unexpected (cf. Fig. 2–13 of Ewing *et al.*, 1957). Another peculiarity is the shape of the  $S_n$  wave. The short period onset of this wave is followed by a signal with much larger period. It is not clear whether this is a second arrival or due to dispersion of the  $S_n$  wave. Professor F. Gilbert has drawn our attention to the possibility that this long-period signal is due to a pseudo-Rayleigh wave at the top of the lower half space, which radiates  $S$  body waves to the surface. (Roever *et al.*, 1959; Gilbert and Laster, 1962). This suggestion is supported by the fact that the phase velocity of this signal is slightly less than the velocity of the  $S_n$  arrival.

In Fig. 5, the first-order discontinuity in the models of Figs. 3 and 4 is replaced by a 1 km thick transition zone. Now, the onset of  $S_n$  has larger amplitudes than in Fig. 4, and the long-period later arrival is reduced in amplitude. This shows that this feature of the  $S_n$  wave depends on the thickness of the transition zone. Up to now,

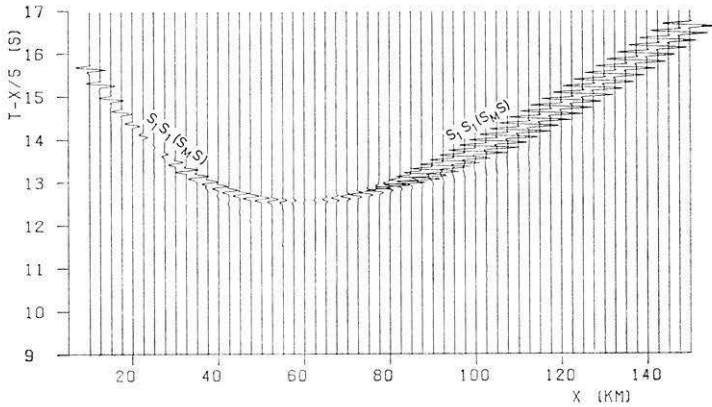


Fig. 3. Theoretical  $SV$ -wave seismograms for a model, consisting of two homogeneous half spaces. The properties of the two media roughly correspond to average velocities and densities of crustal and upper mantle material, respectively ( $\alpha_1 = 6.0$  km/s,  $\beta_1 = 3.46$  km/s,  $\rho_1 = 2.53$  g/cm<sup>3</sup>,  $\alpha_2 = 8.0$  km/s,  $\beta_2 = 4.62$  km/s,  $\rho_2 = 3.28$  g/cm<sup>3</sup>). The double-couple point source and the receivers are located 30 km above the interface between the two media (Moho). The duration of the source signal is 0.15 s. The seismograms are shown on a reduced time scale and correspond to the horizontal displacement in profile direction which is of  $SV$  type alone. On the amplitude scale used, the Moho reflection  $S_1S_1$  (in usual nomenclature  $S_M S$ ) is practically the only arrival that is visible. The amplitudes in Figs. 3–7 should be divided by  $|\sqrt{x}|$  in order to obtain the true amplitudes

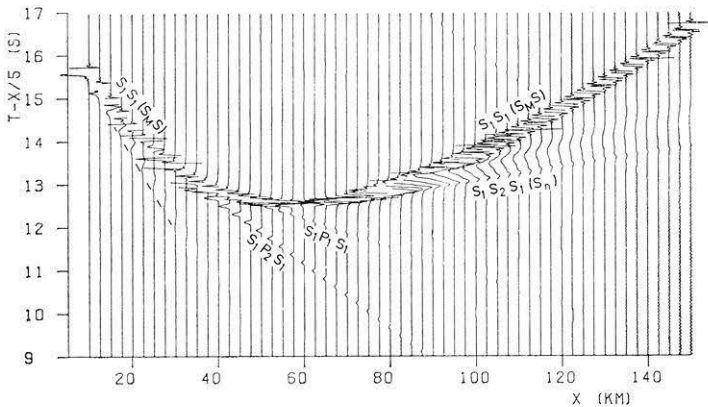


Fig. 4. The same as Fig. 3, but with a tenfold increase in amplitude scale. The amplitudes of the Moho reflection are clipped. Now, three head waves are visible, travelling, respectively, with the  $P$  and the  $S$  velocity of the lower half space ( $S_1P_2S_1$ ,  $S_1S_2S_1$  or  $S_n$ ) and with the  $P$  velocity of the upper half space ( $S_1P_1S_1$ ). The long-period arrival between  $S_n$  and  $S_M S$  is probably due to a pseudo-Rayleigh wave at the top of the lower half space. The arrival marked by the dashed line is a purely numerical effect and travels with the highest phase velocity that is used in the seismogram calculation. Arrivals of this sort are also visible in other seismogram sections of this paper, and they travel with either the highest or the lowest phase velocity

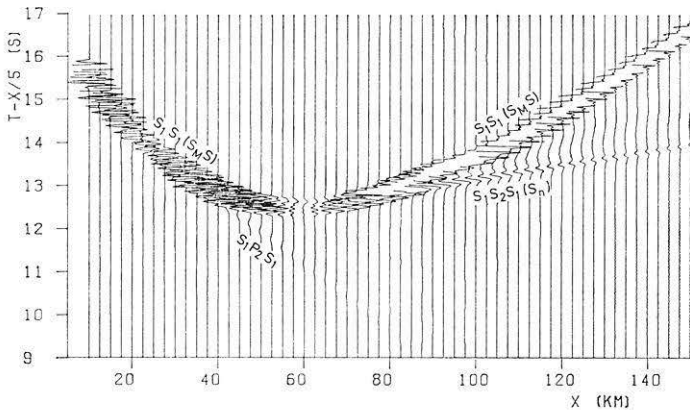


Fig. 5. The same as Fig. 4 for a transition zone with thickness 1 km between the two half spaces. The transition zone is approximated by 4 thin homogeneous layers. The corresponding fine structure determines the Moho reflection for distances up to about 80 km. Beyond, the seismograms resemble those for a linear transition zone

this long-period tail of  $S_n$  has, to our knowledge, not yet been found in observations. The head wave  $S_1P_1S_1$  has disappeared in Fig. 5, indicating that this wave is also closely connected to the sharpness of the crust-mantle transition. The head wave  $S_1P_2S_1$  is reduced in amplitude and has longer periods. This shows that only those long-period parts of the signal are converted into  $P$  waves at the transition zone, for which this zone is still close to a first-order discontinuity.

In Figs. 6 and 7, theoretical  $S$ -wave seismograms for a realistic crustal model of the Rhinegraben area are plotted. The  $P$ -velocity model is taken from Edel *et al.* (1974), and the  $S$ -velocity distribution has the same form. The most prominent phases in Fig. 6 are the reflection  $S_M S$  from the broad crust-mantle transition zone and the head wave  $S_n$ .  $S_n$  is not followed by a long-period signal. This emphasizes that in fact this peculiarity of  $S_n$  is closely related to the sharpness of the crust-mantle transition. At later times and larger distances, there is a multiple reflection between the crust-mantle transition and the top of the basement. A relatively strong phase,  ${}^sP_M P^s$ , appears at earlier times and with higher apparent velocity. This is a wave which travels in the sedimentary layer as an  $S$  wave, is then converted at the top of the basement into a  $P$  wave which is reflected at the crust-mantle transition zone and converted back into an  $S$  wave at the top of the basement. (The occurrence of this wavetype is due to the use of the  $SS$  reflection coefficient. If, for example, the  $SP$  reflection coefficient would be used in order to calculate the  $SP$  response of the model, an even stronger phase  ${}^sP_M P^p$  would be observed.) The same seismograms as in Fig. 6 are plotted in Fig. 7 on a ten times larger amplitude scale. Many more weak multiples and converted phases are now visible. This figure emphasizes the real power of the reflectivity method in that the *complete* response of the model is obtained. In this respect, the reflectivity method is superior to ray-theoretical methods, based on generalized ray theory, where it is not always easy to know which multiples and converted waves should be taken into account. Computed sections like the one in Fig. 7 sometimes pose difficult problems with regard to the interpretation of

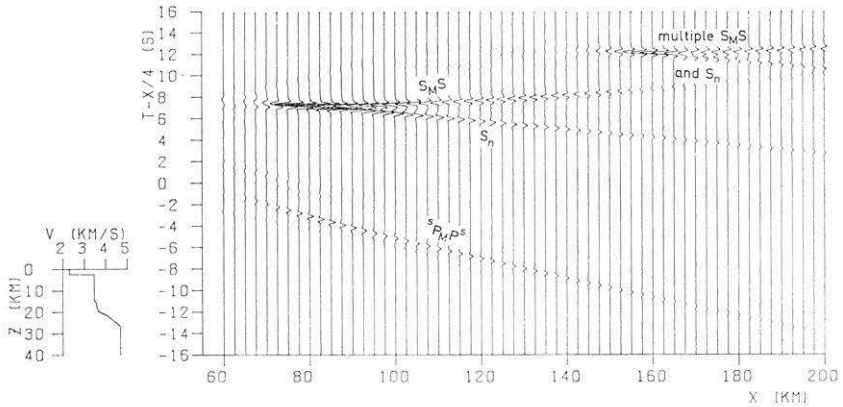


Fig. 6. Theoretical  $SV$ -wave seismograms for a realistic crustal model. The  $S$ -velocity distribution is shown on the left. The seismograms are the complete  $S$  response from the structure below the sedimentary layer due to the  $S$  wave from the double-couple point source. The gradient zones are approximated by homogeneous layers whose thickness is about 1 km. The duration of the source signal is 0.3 s. The main phases are described in the text

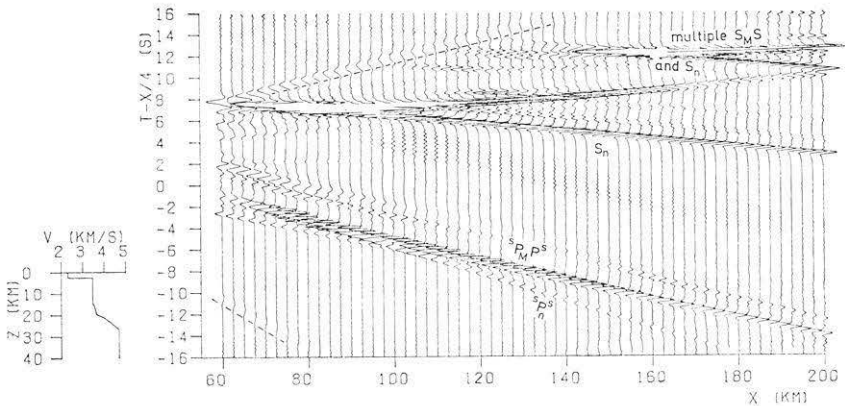


Fig. 7. The same as Fig. 6, but with a tenfold increase in amplitude scale. The amplitudes of the most prominent phases are clipped. Many weak phases due to multiples and conversions in the reflecting zone below the sedimentary layer are now visible. The arrivals along the dashed lines are numerical effects. They are explained in the caption of Fig. 4

multiple and converted waves. We have not studied this question for the section of Fig. 7. The problem will, however, be discussed in greater detail in the next section for models of the whole earth.

Our results for  $S_n$  in different models suggest a simple and perhaps useful way of investigating the thickness of the crust-mantle transition in the real earth. Comparative studies of the frequency content of  $P_n$  and  $S_n$  from near earthquakes with foci in the crust or from explosions could be made, and if substantially more low frequencies are found in  $S_n$  than in  $P_n$  (after correction for the influence of attenuation), then this would point to a relatively sharp transition. If, on the other hand, no essential

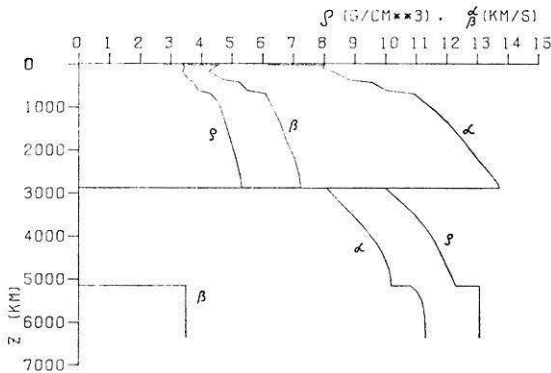


Fig. 8. Earth model A that is used in most calculations of this paper ( $\alpha = P$ -wave velocity,  $\beta = S$ -wave velocity,  $\rho =$  density)

difference in frequency content is found, then, according to our preliminary calculations, the transition should be thicker than roughly the  $S$  wavelength, corresponding to the main frequency of the source pulse. This method could supplement the more obvious method of investigating the Moho reflection  $P_M P$  around the critical point in refraction data.

### *Theoretical Seismograms for Realistic Earth Models*

In this section, synthetic seismograms for  $P$  and  $SV$  phases in realistic earth models will be discussed. The model that is mainly used is based on several recent seismological investigations of the earth's mantle and core (Johnson, 1969; Buchbinder, 1971; Dziewonski and Gilbert, 1971; Press, 1972; Müller, 1973a; Qamar, 1973; Wiggins *et al.*, 1973). This model, called model A in the following, is listed in Table 1 along with a modified version wherein the upper mantle is replaced by the smoother Jeffreys-Bullen upper mantle (Bullen, 1963). Model A is also plotted in Fig. 8. In some cases, the calculations have been performed for models without a crust, i. e., the upper mantle material extends to the earth's surface. Table 2 contains information about all models investigated. The layer thickness given there is the thickness of the homogeneous layers by which the inhomogeneous earth model is approximated. The ratio of  $S$  wavelength to layer thickness varies, in the lower mantle, from about 2 to about 7. The appropriate ratio for modelling an inhomogeneous structure depends on the wave type under investigation and has to be determined by numerical experiments.

The double-couple point source is oriented as in Fig. 1. For rays propagating towards the lower mantle and the core, its  $SV$  radiation is approximately independent of the radiation angle (see Fig. 2). The  $P$  radiation, however, depends strongly on this angle since one of the two nodal planes for  $P$  is vertical. Different values of the main period of the source pulse have been used, as given in Table 2. Source and receivers are located at the same level, corresponding to the earth's surface. The influence of the surface is, however, not taken into account, neither at the source nor at the receivers.

Table 1. Velocity-density distribution

Depth (km)	<i>P</i> velocity (km/s)	<i>S</i> velocity (km/s)	Density (g/cm <sup>3</sup> )
(a) Earth model A			
0	6.20	3.58	2.80
33	6.20	3.58	2.80
33	8.05	4.60	3.45
100	7.95	4.40	3.45
200	8.32	4.25	3.40
380	8.83	4.75	3.60
430	9.56	5.25	3.75
620	10.04	5.50	3.90
700	10.94	6.10	4.30
900	11.29	6.25	4.57
1100	11.64	6.38	4.67
1400	12.07	6.60	4.80
1800	12.56	6.78	4.97
2200	12.99	7.05	5.14
2600	13.48	7.20	5.27
2800	13.69	7.24	5.32
2890	13.73	7.25	5.32
2890	8.10	0	10.00
3200	8.50	0	10.50
3500	8.92	0	10.95
3800	9.31	0	11.30
4000	9.52	0	11.50
4200	9.74	0	11.66
4400	9.91	0	11.80
4600	10.03	0	11.93
4800	10.14	0	12.07
5000	10.19	0	12.21
5162	10.20	0	12.30
5162	10.83	3.50	13.08
5300	11.05	3.50	13.08
5500	11.20	3.50	13.08
5700	11.26	3.50	13.08
5900	11.30	3.50	13.08
6100	11.31	3.50	13.08
6300	11.32	3.50	13.08
6371	11.32	3.50	13.08
(b) Jeffreys Bullen upper mantle			
0	6.20	3.58	2.80
33	6.20	3.58	2.80
33	7.76	4.36	3.32
413	8.97	4.96	3.64
600	10.25	5.66	4.13
800	11.00	6.13	4.49
900	11.29	6.25	4.57

Table 2. Earth models, parameters and computing times

Fig. No.	Earth model	Average layer thickness in km	Main period of source signal in s	Computing time on a UNIVAC 1108
9	model A	100	54	4 h 23 min
10	model A	100	54	2 h 06 min
11	model A	100	30	4 h 04 min
12	model A with JB upper mantle	100	54	2 h 06 min
13 and 14	model A without crust	50	54	6 h 59 min
15	model A with JB upper mantle, without crust	50	17	2 h 12 min

The theoretical record sections in Fig. 9, and Figs. 11 through 15, show the horizontal displacement component in profile direction for the  $SS$  response of the earth models. Fig. 10 is a display of the vertical displacement component of the  $PP$  response. These record sections will be described in some detail in the following. The main point of the discussion will be that besides the main body wave phases such as  $S$ ,  $S_cS$ ,  $SKS$ ,  $SKKS$ ,  $P$ ,  $PKP$  etc. many additional phases are visible. We have been able to identify most of them, and even with regard to the unidentified phases we are sure that they correspond to a physical wave path. Some of these phases may possibly help to determine earth structure in certain depth ranges, provided that they are observed, but most of them only contribute to the background noise for the main phases. Figs. 16 and 17 are schematic diagrams of some of the ray paths associated with the arrivals in the theoretical record sections.

The most energetic phases in Fig. 9 are  $S$  and  $S_cS$  at shorter epicentral distances, and  $SKS$  and  $SKKS$  at larger distances. Many additional phases may be detected in this section. They arrive earlier or later than the main phases, and in most cases they have less energy. These phases are due to multiple reflections and converted wave types at various discontinuities and transition zones of the model. The crust-mantle boundary (Moho) and the core-mantle boundary are the two major discontinuities of the model. One multiple between these boundaries may be recognized. It is marked  $S_cSmS_cS$ . The letter  $m$  stands for reflection at the Moho and was introduced to distinguish this phase from the multiple at the free surface,  $S_cSS_cS$ , which would arrive a few seconds later with larger amplitudes.  $S_cSS_cS$  does not appear in the seismograms since in the present version of our computer program there is no possibility to include reflectors above the source. Similarly, a phase  $S_mS$  is seen in the synthetic seismograms with travel times close to those of  $SS$ . Phases arriving earlier than  $S$  and  $SKS$  and phases arriving between  $SKKS$  and  $S_mS$  will be discussed later in connection with Fig. 11.

The prominent phases in the  $P$ -wave seismogram section of Fig. 10 are  $P$ ,  $P_{diff}$  and  $PKP$ .  $P_cP$  has very small amplitudes at short distances and is therefore difficult to detect on the amplitude scale used. At larger distances, it interferes with other

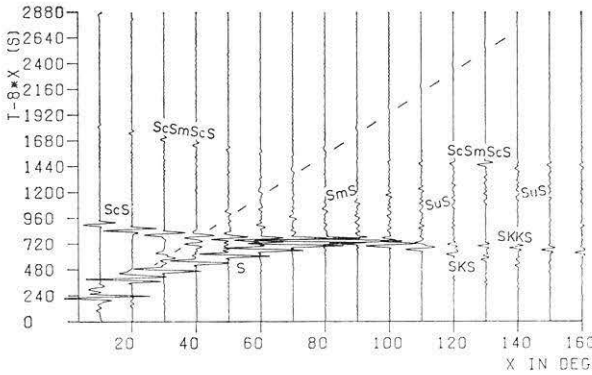


Fig. 9. *SS* response of model A (horizontal displacement in profile direction). The main period of the source pulse is 54 s. For an explanation of the various phases, see the text and Figs. 16 and 17. The arrival along the dashed line is a numerical effect and is explained in the caption of Fig. 4. The amplitudes in Figs. 9–15 should be divided by  $|\sin x|$  in order to obtain the true amplitudes

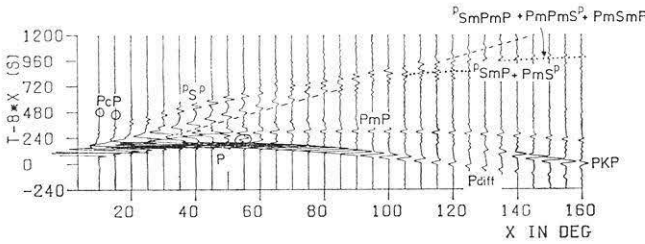


Fig. 10. *PP* response of model A (vertical displacement). The main period of the source pulse is 54 s. The encircled arrival in the seismogram at 55° is *PcP*. After division by 4, the amplitudes are on the same scale as the *S*-wave amplitudes in Fig. 9

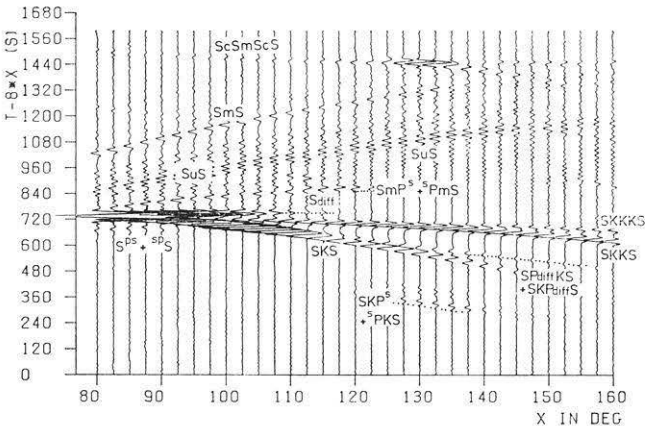


Fig. 11. *SS* response of model A for a source pulse with main period 30 s (horizontal displacement in profile direction)

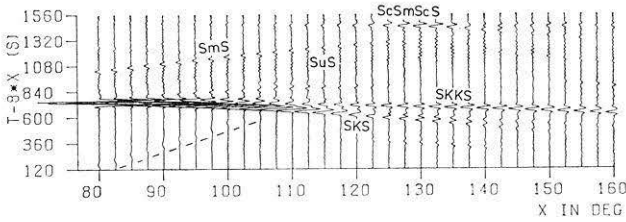


Fig. 12.  $SS$  response of model A with a smooth upper mantle, corresponding to the Jeffreys-Bullen earth model. The source pulse has a length of 54 s.  $SuS$  is much weaker than in Fig. 11 where model A has been used throughout

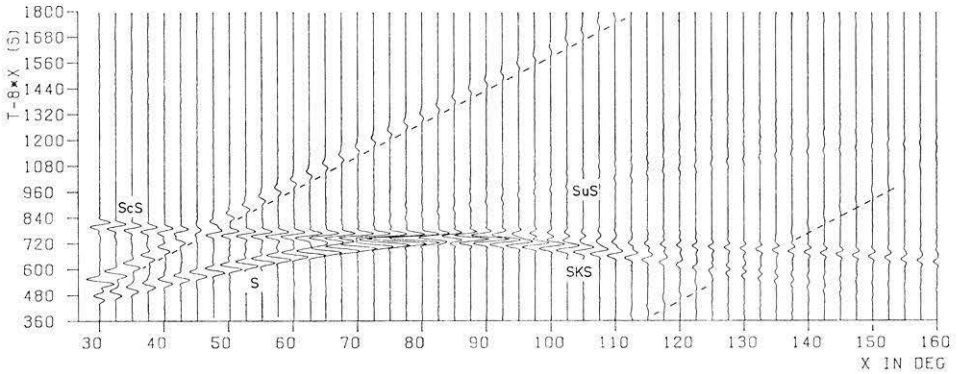


Fig. 13.  $SS$  response of model A with the crust removed. The average layer thickness is 50 km, and the source-pulse length is 54 s. Since the model has no Moho, multiples such as  $SmS$  and  $ScSmScS$  are missing. Because of the small layer thickness, compared to the wavelength,  $SuS$  is a good approximation of the true pulse

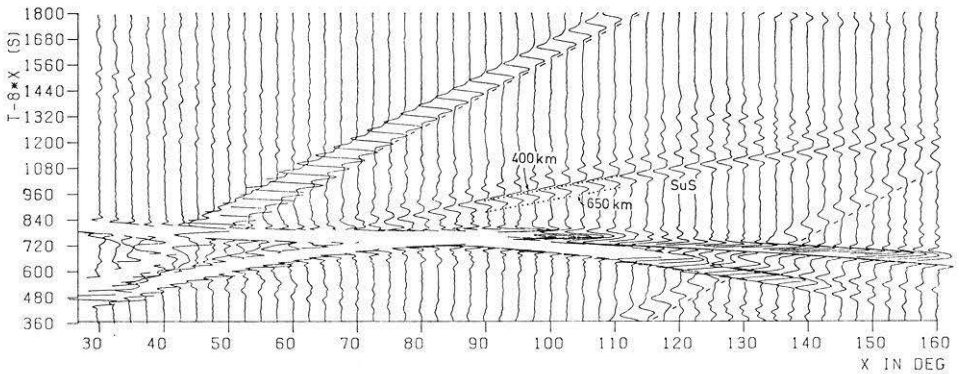


Fig. 14. The same as Fig. 13, but on a ten times larger amplitude scale. The two dotted lines approximately give the theoretical travel times of the  $SuS$  contribution from the 400 km and the 650 km transition zone, respectively. They are based on the Jeffreys-Bullen travel time tables for  $S$  waves from deep-focus earthquakes. The shift of some arrivals from the end of the seismograms to the beginning and vice versa beyond  $110^\circ$  is due to aliasing in the time domain

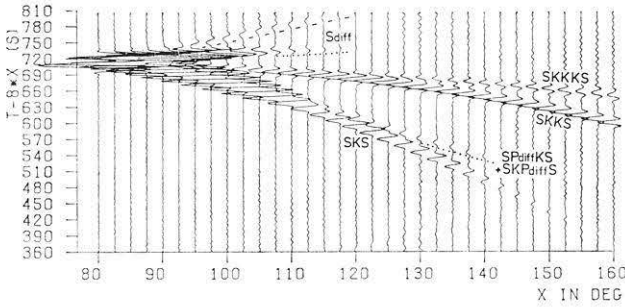


Fig. 15. *SS* response of model A with a smooth upper mantle and no crust, including mainly *SKS*, *SKKS* and *SKKKS*, for a relatively short duration of the source pulse, namely 17 s. The forms of *SKS*, *SKKS* and *SKKKS* are quite different. The causes are discussed in the text

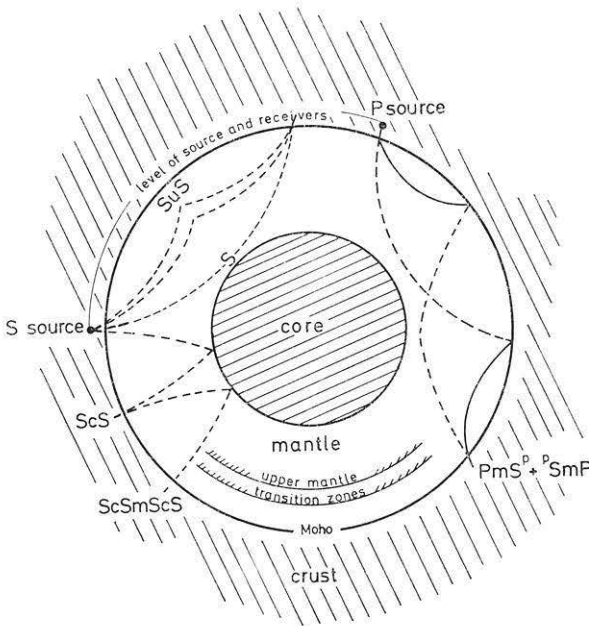


Fig. 16. Ray-path diagrams of some of the phases, appearing in Figs. 9 through 15. *S*-wave segments are dashed, *P*-wave segments are full lines

arrivals except at  $55^\circ$  where it is clearly visible. *PmP*, which is analogous to *SmS* in Fig. 9, can be recognized instead of *PP*. Another wave train at later times and with lower apparent velocity can be seen. This wave train consists of various converted and multiple wave types such as  $vS^p$ ,  $vSmP$ ,  $PmS^p$ ,  $vSmPmP$ ,  $PmPmS^p$  and  $PmSmP$ . The superscript *p* stands for a wave travelling in the crust as a *P* wave with conversion into or from *S* at the Moho. These waves are close in travel time, but not in amplitude, to *S*, *SP*, *PS*, *SPP*, *PPS* and *PSP*, respectively. Examples of these phases are illustrated in the ray-path diagram of Fig. 16.

Fig. 11 shows an *SV*-wave seismogram section for model A and for a source pulse with duration 30 s. This duration is shorter than that used in the calculation

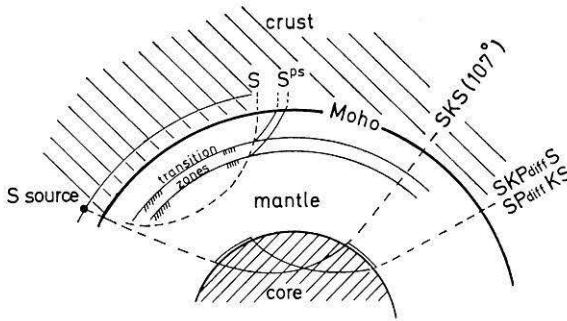


Fig. 17. Some more ray paths

for Fig. 9 and thus gives a better time resolution. In addition, the receiver spacing has been decreased which makes it easier to follow phases. The phases  $SmP^s + sPmS$  and  $SKP^s + sPKS$  arrive close to the onset times of  $SP + PS$  and  $SKP + PKS$ , respectively, but have different amplitudes. The superscript  $s$  denotes a crustal  $S$ -wave segment of the ray either before or after conversion at the Moho. In addition to these phases, a very quickly decaying  $S_{diff}$ , and  $SKKS$  are visible in Fig. 11. The influence of the structure in the upper mantle also becomes very obvious. Most of the energy between  $S$ ,  $S_{diff}$  and  $SmP^s + sPmS$  on the one hand and  $Sms$  on the other is due to reflections from the transition zones in the upper mantle. These phases are called  $SuS$  in Fig. 11, and their rays are illustrated in Fig. 16. The ringing character of  $SuS$  is explained by the fact that the average layer thickness in the mantle of model A is, for these phases, not small enough relative to the dominant wavelength of the signal. Thus,  $SuS$  does not correspond to the inhomogeneous model A, but only to its approximation by discrete layers. However, the large amplitude wave group in the middle of the ringing wave train which corresponds to reflections from the two transition zones centered around depths of 400 km and 650 km, respectively, indicates that  $SuS$  for the inhomogeneous model is not negligibly small. This will later be confirmed in connection with Figs. 13 and 14. The transition zones in the upper mantle cause further phases. For example, forerunners to  $S$  between  $80^\circ$  and  $90^\circ$  epicentral distance are due to the conversion of portions of the energy of  $S$  into  $P$  waves at these transition zones. These forerunners travel through the crust as  $S$  waves once more, since only  $S$  waves in the crust are included in the calculations. They may therefore be called  $S^{ps}$ , and forerunners of the type  $spS$  are likewise included. The ray path of  $S^{ps}$  is illustrated in Fig. 17. Similarly, the arrivals about 50 s after  $SKP^s + sPKS$  are caused by the conversion of  $P$  waves into  $S$  waves and vice versa at the upper mantle transition zones. However, perhaps the most interesting aspect of Fig. 11 is the phase labelled  $SP_{diff}KS + SKP_{diff}S$  which has, to our knowledge, not yet been reported from observations. The two ray paths of this phase are shown in Fig. 17. Both of them include a  $P$ -wave portion diffracted along the core-mantle boundary. The travel-time curve of this phase is a straight line with the slope of  $P_{diff}$  and tangential to the travel-time curve of  $SKS$  at a distance of  $107^\circ$ . This diffracted wave produces strong pulse deformations of  $SKS$  in the distance range around  $120^\circ$  where it separates from  $SKS$ .

Figs. 12 to 14 show further investigations of  $SuS$ . The model used for Fig. 12 has a smooth upper mantle with Jeffreys' velocity distributions and Bullen's density distribution A (Bullen, 1963). As shown in Table 2, the average layer thickness is the same as that used for Fig. 11, but the dominant period of the source pulse, 54 s, is almost twice the value for that figure. Because of the greater wavelength to layer thickness ratio the ringing character of  $SuS$  is reduced, but its generally smaller amplitudes are mainly due to the smoothness of the upper mantle model used. In order to determine  $SuS$  correctly for model A, a calculation with an average layer thickness of 50 km was performed (Figs. 13 and 14). For a source pulse with main period 54 s this is, in the transition region of the upper mantle, about one sixth of the  $S$  wavelength. Ringing has now disappeared, and  $SuS$  is close to the true reflection from the upper mantle transition zones, i. e., further reduction of the layer thickness would not change it essentially. At epicentral distances up to  $110^\circ$ ,  $SuS$  consists mainly of the reflections from the two transition zones at depths of 400 and 650 km. At larger distances, there are some more oscillations in  $SuS$  which are reflections from the depth range of the pronounced low-velocity zone in the  $S$ -velocity distribution (see Fig. 8).

An interesting feature of the phases  $SKS$ ,  $SKKS$  and  $SKKKS$  is their strong difference in wave form. This is especially evident from Fig. 15 where the shortest of all pulse lengths, 17 s, has been used, thus giving clearly separated arrivals. The reasons for the differences in pulse form are that the rays of  $SKKS$  and  $SKKKS$  touch caustics in the outer core whereas the rays of  $SKS$  do not, and that there are partly phase shifts upon transmission and reflection at the core-mantle boundary. Choy and Richards (1975) have discussed these effects in general and given approximate transformations which relate the shapes of phases such as  $sS$  and  $SS$  from deep focus earthquakes, or  $SKS$  and  $SKKS$ . They assume that  $sS$  and  $SKS$  have not suffered essential wave-form changes along their paths. For  $SKS$  at distances around  $120^\circ$ , however, the diffracted wave  $SP_{\text{diff}}KS + SKP_{\text{diff}}S$  actually produces severe deformations in  $SKS$ , as is seen in Figs. 11 and 15, and it is just in this distance range that Choy and Richards apply their transformation method to longperiod  $WWNSS$  records of  $SKS$  and  $SKKS$ . Besides noise of different origin in the data, this is probably a major reason why this method, which certainly takes correct account of the main causes of pulse deformation, does not give particularly satisfactory results. From the seismograms in Fig. 15, more suitable distance ranges for this method appear to be the interval from  $100^\circ$  to  $110^\circ$  approximately and distances around  $140^\circ$  where  $SP_{\text{diff}}KS + SKP_{\text{diff}}S$  has separated from  $SKS$ , and  $SKKKS$  from  $SKKS$ . Two of the observed seismograms in Choy's and Richards' paper resemble so closely the theoretical seismogram at the distance  $117.5^\circ$  in Fig. 15 that we have drawn them on the same time scale in Fig. 18 in order to demonstrate the agreement between observation and theory that can be achieved.

### *Summary and Conclusions*

The reflectivity method for the calculation of theoretical seismograms has been extended to include a double-couple point source and to compute  $SV$ -wave seismograms, using the  $SS$  reflection coefficient of a layered medium. Synthetic seismograms of  $SV$  waves have been computed for crustal models and for models of the whole

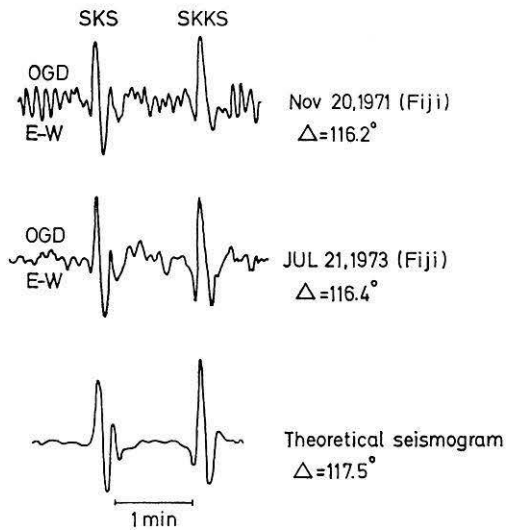


Fig. 18. Comparison of observed and theoretical seismograms for  $SKS$  and  $SKKS$ . The observed seismograms are from a paper by Choy and Richards (1975) and represent the long-period E–W component at the  $WWNSS$  station Odgensburg, New Jersey, U.S.A. With respect to the epicenters, this component is practically radial and therefore directly comparable with the theoretical seismogram which was taken from Fig. 15. Correcting the epicentral distances for the effect of focal depth gives an increase of  $0.8^\circ$  to  $1^\circ$  and thus values close to  $117.5^\circ$ . The data of the two earthquakes are: (1) November 20, 1971, 07:28:01.1;  $23.4^\circ$  S,  $179.9^\circ$  W; depth 551 km;  $m_b = 6.0$ . (2) July 21, 1973, 04:19:17.1,  $24.8^\circ$  S,  $179.2^\circ$  W; depth 411 km;  $m_b = 5.9$

earth. These calculations gave the complete  $SV$ -wave response of the models, including multiple reflections and conversions. Since such phases, for instance  $SKKS$  and  $SKKKS$ , are sometimes of considerable interest in seismology, the reflectivity method has a broader field of applications in seismic body-wave studies than generalized ray theory. This advantage is, however, accompanied by the requirement of relatively long computing times.

For a model of two half spaces, separated by a first-order discontinuity and having average properties of the earth's crust and upper mantle, respectively, we found two unfamiliar types of  $SV$  head waves, one travelling with the  $P$  velocity of the upper half space, and one which is slightly slower than the head wave travelling with the  $S$  velocity of the lower half space. The second of these head waves has unusually low frequencies and is probably caused by a pseudo-Rayleigh wave at the top of the lower half space. Both head waves eventually disappear if the discontinuity between the half spaces is replaced by transition zones of increasing thickness. Models of the whole earth also produce  $SV$  phases that are not always expected. One is the diffracted wave  $SP_{\text{diff}}KS + SKP_{\text{diff}}S$  whose travel-time curve is a straight line tangential to the travel-time curve of  $SKS$ . It interferes strongly with  $SKS$  in the distance range around  $120^\circ$ .

Another result of our calculations is that the structure of the upper mantle is quite important for various types of multiples and converted waves. We have identified reflections  $S\mu S$  from the transition zone region of our earth model A,

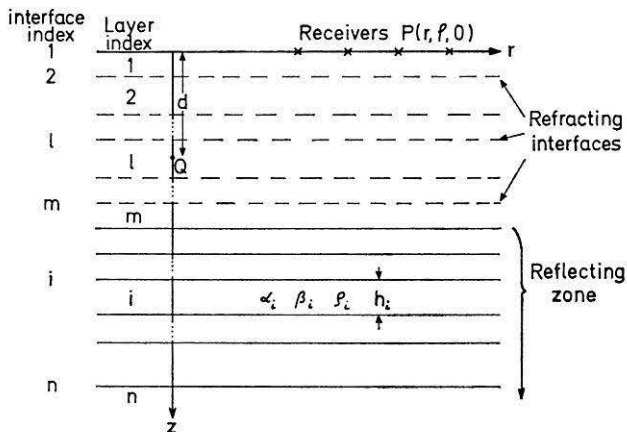


Fig. A-1. The layered medium with the double-couple point source

produced by  $S$  waves incident from below, and forming forerunners to  $SS$ . Moreover, there are forerunners to  $S$  due to conversions from  $S$  to  $P$  waves in this region. The existence of these various forerunners depends strongly on the sharpness of the transition zones in the upper mantle, and therefore they might be used in checking proposed velocity and density distributions.

The main  $S$ -wave phases,  $S$ ,  $S\epsilon S$ ,  $SKS$  and  $SKKS$ , are the prominent arrivals in our  $S$ -wave seismogram sections, and the phases mentioned in the preceding paragraphs, as interesting as they are, are almost all quite weak in comparison. The final purpose of the present work is to compare observed long-period and theoretical seismograms for the main  $S$  phases. This comparison should show whether or not present earth models are, in their lower mantle and outer core part, compatible with the amplitudes and signal shapes of these phases. Besides that, it will be of interest to search in data for some of the minor phases mentioned above.

*Acknowledgements.* This research was supported by a grant from the Deutsche Forschungsgemeinschaft. The extensive calculations were performed at the computing center of the University of Karlsruhe and on the computer of the Geophysical Institute. Our work on the latter was greatly supported by Werner Kaminski. We are grateful to David Bamford and Karl Fuchs for reading the manuscript and for discussions, and to George Choy and Paul Richards for a preprint of their paper. The manuscript was typed by Ingrid Hörnchen.

#### *Appendix A: Reflectivity Method for a Double-Couple Point Source*

In this appendix, a compact description of the reflectivity method for a double-couple point source is given, including all necessary formulas. Fig. A-1 shows the geometry of the layered medium. It is subdivided into the reflecting zone and a stack of  $m$  surficial layers which produce only time shifts and elastic transmission losses. The source  $Q$  is assumed to lie inside one of the layers 1 through  $m$ . Two coordinate systems are used; cylindrical coordinates  $r$ ,  $\varphi$ ,  $z$  for the receivers and the displacement components  $u_r$ ,  $u_\varphi$ ,  $u_z$ , and cartesian coordinates  $x_1$ ,  $x_2$ ,  $x_3$  for describing the orientation of the double couple (Fig. A-2). The unit vectors  $\mathbf{f} = (f_1, f_2, f_3)$  and  $\mathbf{n} = (n_1, n_2, n_3)$  are those normals to the  $P$  nodal planes that have between them one of

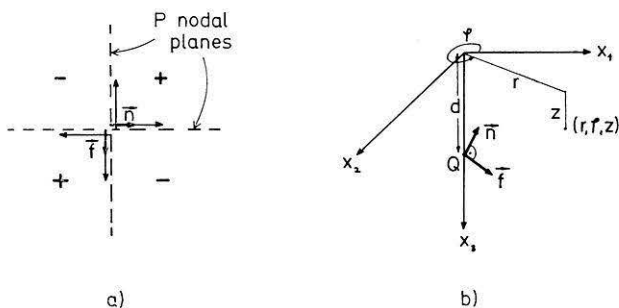


Fig. A-2. a) Unit vectors  $\mathbf{f}$  and  $\mathbf{n}$ , describing the double couple. The plus and minus signs denote first  $P$  motions away and towards the source, respectively. b) Cylindrical and cartesian coordinates that are used, and the unit vectors  $\mathbf{f}$  and  $\mathbf{n}$  of the double couple

the quadrants with first  $P$  motions *towards* the source. (Instead of  $\mathbf{f}$  and  $\mathbf{n}$ ,  $-\mathbf{f}$  and  $-\mathbf{n}$  can also be used.) In practical applications, these vectors can be derived from fault-plane solutions of earthquakes.

The starting point of the derivation is a paper by Müller (1969) on generalized ray theory for single-force and dipole point sources. The expressions (13) of that paper give the complete displacements, corresponding to an arbitrary generalized ray from a harmonic single-force point source to the receiver. We have used these expressions and the transformation formulas (19) in the same paper to derive the displacements due to a single couple. Superposing the displacements due to a second single couple gives the displacements due to a harmonic double couple. In the whole derivation, near-field terms are dropped which essentially means that  $P$  and  $SV$  waves have no azimuthal displacement  $u_\varphi$ , and  $SH$  waves no radial displacement  $u_r$ . This neglect is fully justified in view of practical applications. The resulting displacements are then specialized for the following generalized rays:

- a)  $SH$  ray from the source  $Q$  to the top of the reflecting zone (RZ) and from RZ to the receiver  $P$  ( $SH$  response)
- b)  $P$  ray from  $Q$  to RZ and from RZ to  $P$  ( $PP$  response)
- c)  $P$  ray from  $Q$  to RZ,  $SV$  ray from RZ to  $P$  ( $PS$  response)
- d)  $SV$  ray from  $Q$  to RZ and from RZ to  $P$  ( $SS$  response)
- e)  $SV$  ray from  $Q$  to RZ,  $P$  ray from RZ to  $P$  ( $SP$  response)

These displacements contain the generalized reflection coefficients, in the sense of generalized ray theory, of the interface on top of the reflecting zone. Replacing these interface reflection coefficients by the reflection coefficients (or reflectivities) of the *whole reflecting zone* gives the displacements according to the reflectivity method. They are given in the following in the form of Fourier transforms for an arbitrary double-couple moment function  $M(t)$ . Because of their derivation from generalized ray theory, they are integrals over the apparent slowness  $u$ . The angle of incidence at the top of the reflecting zone,  $\gamma$ , is introduced at the end.

The following abbreviations are used in the displacement formulas:

$$\begin{aligned}
 \gamma_1 &= f_1 \cos \varphi + f_2 \sin \varphi & \gamma_2 &= -f_1 \sin \varphi + f_2 \cos \varphi & \gamma_3 &= f_3 \\
 \delta_1 &= n_1 \cos \varphi + n_2 \sin \varphi & \delta_2 &= -n_1 \sin \varphi + n_2 \cos \varphi & \delta_3 &= n_3 \\
 q_j &= (u^2 - \alpha_j^{-2})^{\frac{1}{2}} & q_j' &= (u^2 - \beta_j^{-2})^{\frac{1}{2}}
 \end{aligned}$$

Table A-1. The functions  $F_1(u)$ ,  $F_2(u)$ ,  $F_3(u)$ 

Type of wave at receiver	Free surface included?	$F_1(u)$	$F_2(u)$	$F_3(u)$
$SH$	no	1	—	—
	yes	2	—	—
$P$	no	—	1	$-\frac{q_1}{u}$
	yes	—	$\frac{4 \beta_1^2 q_1 q_1'}{D(u)}$	$-\frac{q_1}{u} \cdot \frac{4 \beta_1^2 u^2 - 2}{D(u)}$
$SV$	no	—	$\frac{q_1'}{u}$	-1
	yes	—	$\frac{q_1'}{u} \cdot \frac{4 \beta_1^2 u^2 - 2}{D(u)}$	$-\frac{4 \beta_1^2 q_1 q_1'}{D(u)}$

$$D(u) = 4 \beta_1^4 u^2 q_1 q_1' - (2 \beta_1^2 u^2 - 1)^2$$

The radicals  $q_j$  and  $q_j'$  are positive imaginary for real  $u$  from  $u=0$  to  $u=\alpha_j^{-1}$  and  $u=\beta_j^{-1}$ , respectively.

#### $SH$ Wave at Receiver

$$\bar{u}_r = 0$$

$$\bar{u}_\varphi = -\frac{\omega^2 \bar{M}(\omega)}{4\pi \varrho_l \beta_l^2} \int_0^\infty \left[ (\delta_3 \gamma_2 + \delta_2 \gamma_3) u J_0(u\omega r) + (\delta_1 \gamma_2 + \delta_2 \gamma_1) \frac{u^2}{q_l'} J_1(u\omega r) \right] P'(\omega, u) F_1(u) e^{\varrho(u)\omega} du \quad (A-1)$$

$$\bar{u}_z = 0$$

Here we have:

$$P'(\omega, u) = \prod_{l=1}^m t_j^+(u) \times \prod_2^m t_j^-(u) \times r_{ss}(\omega, \gamma(u))$$

$t_j^+(u)$  and  $t_j^-(u)$  are plane-wave transmission coefficients for the  $j$ -th interface, corresponding to downward and upward propagation, respectively:

$$t_j^+(u) = 2 \varrho_{j-1} \beta_{j-1}^2 q_{j-1}' / N(u) \quad t_j^-(u) = 2 \varrho_j \beta_j^2 q_j' / N(u)$$

$$N(u) = \varrho_{j-1} \beta_{j-1}^2 q_{j-1}' + \varrho_j \beta_j^2 q_j'$$

$r_{ss}(\omega, \gamma(u))$  is the  $SH$  reflectivity of the reflecting zone and depends on both frequency and apparent velocity or angle of incidence. It can be calculated by matrix

Table A-2. The functions  $A(u)$  and  $B(u)$ 

Type of wave at receiver	$A(u)$	$B(u)$
$P$	$\frac{\delta_1 \gamma_3 + \delta_3 \gamma_1}{2 \pi q_l} u^3$	$\frac{\delta_3 \gamma_3 - \delta_1 \gamma_1}{2 \pi q_l} \cdot \frac{u^4}{q_l} - \frac{\delta_3 \gamma_3}{2 \pi q_l \alpha_l^2} \cdot \frac{u^2}{q_l}$
$SV$	$\frac{\delta_1 \gamma_3 + \delta_3 \gamma_1}{4 \pi q_l} \cdot \frac{(2u^2 - \beta_l^{-2}) u^2}{q_l'}$	$\frac{\delta_3 \gamma_3 - \delta_1 \gamma_1}{2 \pi q_l} u^3$

 Table A-3. The functions  $P(\omega, u)$  and  $g(u)$ 

Response	$P(\omega, u)$	$g(u)$
$PP$	$\prod_{l+1}^m T_j^+(u) \times \prod_2^m T_j^-(u) \times R_{pp}(\omega, \gamma(u))$	$H q_l - \sum_1^m b_j q_j - \sum_{l+1}^m b_j q_j$
$PS$	$\prod_{l+1}^m T_j^+(u) \times \prod_2^m U_j^-(u) \times R_{ps}(\omega, \gamma(u))$	$H q_l - \sum_1^m b_j q_j' - \sum_{l+1}^m b_j q_j$
$SS$	$\prod_{l+1}^m U_j^+(u) \times \prod_2^m U_j^-(u) \times R_{ss}(\omega, \gamma(u))$	$H q_l' - \sum_1^m b_j q_j' - \sum_{l+1}^m b_j q_j'$
$SP$	$\prod_{l+1}^m U_j^+(u) \times \prod_2^m T_j^-(u) \times R_{sp}(\omega, \gamma(u))$	$H q_l' - \sum_1^m b_j q_j - \sum_{l+1}^m b_j q_j'$

$$H = d - \sum_1^l b_j$$

methods. The function  $F_1(u)$  depends on whether or not the influence of the free surface is to be taken into account at the receivers. It is given in Table A-1. The function  $g(u)$  is the same as that for the  $SS$  response in Table A-3.

*P or SV Wave at the Receiver*

$$\bar{u}_r = \omega^2 \bar{M}(\omega) \int_0^\infty [-A(u) J_0(u\omega r) + B(u) J_1(u\omega r)] P(\omega, u) F_2(u) e^{\sigma(u)\omega} du \quad (A-2)$$

$$\bar{u}_\varphi = 0$$

$$\bar{u}_z = \omega^2 \bar{M}(\omega) \int_0^\infty [A(u) J_1(u\omega r) + B(u) J_0(u\omega r)] P(\omega, u) F_3(u) e^{\sigma(u)\omega} du \quad (A-3)$$

The functions  $A(u)$  and  $B(u)$  depend on whether  $P$  or  $SV$  radiation at the source is considered. They are given in Table A-2. The functions  $F_2(u)$  and  $F_3(u)$  are analogous to  $F_1(u)$  in the case of  $SH$  waves. They are given in Table A-1. The functions  $P(\omega, u)$  and  $g(u)$  depend on the type of interaction with the reflecting zone and are compiled in Table A-3. The functions  $T_j^+(u)$  and  $T_j^-(u)$  are plane-wave transmission

coefficients for  $P$  waves and for downward and upward propagation, respectively,  $U_j^+(u)$  and  $U_j^-(u)$  are the corresponding  $SV$  transmission coefficients. These coefficients are as follows:

$$\begin{aligned} T_j^+(u) &= 2 \varrho_{j-1} q_{j-1} [(cu^2 - \varrho_{j-1}) q_j' - (cu^2 + \varrho_j) q_{j-1}'] / O(u) \\ U_j^+(u) &= 2 \varrho_{j-1} q_{j-1}' [(cu^2 - \varrho_{j-1}) q_j - (cu^2 + \varrho_j) q_{j-1}] / O(u) \\ T_j^-(u) &= \frac{\varrho_j q_j}{\varrho_{j-1} q_{j-1}} T_j^+(u) \quad U_j^-(u) = \frac{\varrho_j q_j'}{\varrho_{j-1} q_{j-1}'} U_j^+(u) \\ O(u) &= u^2(cu^2 - \varrho_{j-1} + \varrho_j)^2 - q_j q_j'(cu^2 - \varrho_{j-1})^2 - q_{j-1} q_{j-1}'(cu^2 + \varrho_j)^2 \\ &\quad - \varrho_{j-1} \varrho_j (q_j q_{j-1}' + q_{j-1} q_j') + c^2 u^2 q_{j-1} q_j q_{j-1}' q_j' \\ c &= 2(\varrho_{j-1} \beta_{j-1}^2 - \varrho_j \beta_j^2) \end{aligned}$$

The  $P$ - $SV$  reflectivities  $R_{pp}$ ,  $R_{ps}$ ,  $R_{ss}$  and  $R_{sp}$  of the reflecting zone are calculated by matrix methods. Appendix B gives some details.

For the numerical integration of expressions such as (A-2), the angle of incidence at the top of the reflecting zone,  $\gamma$ , is introduced by the relation

$$u = \frac{\sin \gamma}{c} \tag{A-4}$$

where  $c = \alpha_m$  for the  $PP$  and  $PS$  response, and  $c = \beta_m$  for the  $SH$ ,  $SS$  and  $SP$  response. The numerical integration is performed, using equidistant and real values of  $\gamma$ . The restriction to real  $\gamma$  gives the body-wave response in the corresponding range of apparent velocities. More details about the numerical calculation can be found in Fuchs and Müller (1971). For the special orientation of the double couple, used in the main part of this paper, and for  $m=1$ , formulas (A-2) and (A-3) reduce, after introduction of (A-4), to expressions (1) through (4).

### Appendix B: Calculation of $SS$ and $SP$ Reflection Coefficients

Reflection and transmission coefficients of plane elastic waves for a horizontally layered medium between two half spaces have been calculated, among others, by Fuchs (1968a) and Červený (1974), using the methods of Haskell (1953) and Dunkin (1965). The desired  $SS$  and  $SP$  reflection coefficients,  $R_{ss}$  and  $R_{sp}$ , may be calculated directly from the elements of the Haskell matrix  $M$ . This matrix is given by Fuchs (1968a) in the following form:

$$M = T_n^{-1} \cdot G_{n-1} \cdot \dots \cdot G_1 \cdot T_0$$

where  $T_n^{-1}$ ,  $G_i$  and  $T_0$  are the matrices of the lower half space, the  $i$ -th layer and the upper half space, respectively. The elements of these matrices are also given by Fuchs (1968a). However, since numerical difficulties may arise from a direct application of the Haskell matrix, Dunkin's matrix method which avoids these difficulties is usually used. The elements of Dunkin's  $6 \times 6$  matrix  $\hat{M}$  are all possible  $2 \times 2$  subdeterminants of the  $4 \times 4$  Haskell matrix  $M$ .  $\hat{M}$  is called the delta matrix of  $M$

(Červený, 1974). The construction of delta matrices is described in detail by Fuchs (1968a) and Červený (1974). Since the delta matrix of a product of matrices is equal to the product of their delta matrices, the delta matrices  $\hat{T}_n^{-1}$ ,  $\hat{G}_i$  and  $\hat{T}_0$  of  $T_n^{-1}$ ,  $G_i$  and  $T_0$  may be used instead of these matrices themselves. Červený (1974) has calculated  $R_{ss}$  and  $R_{sp}$  in terms of the elements  $\hat{M}_{ij}$  of the Dunkin matrix  $\hat{M}$ :

$$R_{sp} = \hat{M}_{15}/\hat{M}_{11} \quad R_{ss} = -\hat{M}_{13}/\hat{M}_{11}$$

For the calculation of  $\hat{M}_{11}$ ,  $\hat{M}_{13}$  and  $\hat{M}_{15}$ , only the first row of  $\hat{T}_n^{-1}$ , the complete delta matrices  $\hat{G}_i$ , and the first, third and fifth column of  $\hat{T}_0$  are needed. Most of these quantities, i.e. all but the third and fifth column of  $\hat{T}_0$ , are given by Fuchs (1968a). The elements of the third and fifth column of  $\hat{T}_0$  are:

$$\begin{aligned} (\hat{T}_0)_{13} &= -k^2 + \nu_0 \nu'_0 & (\hat{T}_0)_{15} &= 2 \nu'_0 k \\ (\hat{T}_0)_{23} &= i \nu'_0 \mu_0 (2k^2 - l_0) & (\hat{T}_0)_{25} &= 0 \\ (\hat{T}_0)_{33} &= -i k \mu_0 (l_0 - 2\nu_0 \nu'_0) & (\hat{T}_0)_{35} &= 2 i \nu'_0 \mu_0 l_0 \\ (\hat{T}_0)_{43} &= (\hat{T}_0)_{33} & (\hat{T}_0)_{45} &= 4 i \nu'_0 \mu_0 k^2 \\ (\hat{T}_0)_{53} &= i \nu_0 \mu_0 (2k^2 - l_0) & (\hat{T}_0)_{55} &= 0 \\ (\hat{T}_0)_{63} &= \mu_0^2 (4k^2 \nu_0 \nu'_0 - l_0^2) & (\hat{T}_0)_{65} &= 4 \mu_0^2 \nu'_0 k l_0 \end{aligned}$$

with

$$\begin{aligned} \mu_0 &= \beta_0^2 \rho_0 & \nu_0 &= \begin{cases} (k_{\alpha_0}^2 - k^2)^{\frac{1}{2}}, & k_{\alpha_0} \geq k \\ -i(|k_{\alpha_0}^2 - k^2|)^{\frac{1}{2}}, & k_{\alpha_0} < k \end{cases} \\ l_0 &= 2k^2 - k_{\beta_0}^2 & \nu'_0 &= \begin{cases} (k_{\beta_0}^2 - k^2)^{\frac{1}{2}}, & k_{\beta_0} \geq k \\ -i(|k_{\beta_0}^2 - k^2|)^{\frac{1}{2}}, & k_{\beta_0} < k \end{cases} \\ k_{\beta_0} &= \omega/\beta_0 \\ k_{\alpha_0} &= \omega/\alpha_0 \end{aligned}$$

and wavenumber  $k$ , circular frequency  $\omega$ , and density  $\rho_0$ ,  $P$  velocity  $\alpha_0$  and  $S$  velocity  $\beta_0$  in the upper half space. In these formulas, we have retained the original numbering of the layers, used by Fuchs (1968a), which differs from the numbering in this paper. In applications, the index zero above has to be replaced by the index  $m$  of the layer immediately on top of the reflecting zone. The relation between wavenumber  $k$  and apparent slowness  $u$ , as used in this paper, is  $k = u\omega$ .

### References

Buchbinder, G.G.R.: A velocity structure of the earth's core. *Bull. Seism. Soc. Am.* 61, 429–456, 1971  
 Buchbinder, G.G.R.: Diffraction from the PKP caustic B. *Bull. Seism. Soc. Am.* 64, 33–43, 1974  
 Bullen, K.E.: An introduction to the theory of seismology. Third ed. London: Cambridge University Press 1963  
 Červený, V.: Reflection and transmission coefficients for transition layers. *Studia geoph. et geod.* 18, 59–68, 1974  
 Chapman, C.H.: The earth flattening transformation in body wave theory. *Geoph. J. R. A. S.* 35, 55–70, 1973  
 Choy, G.L., Richards, P.G.: Pulse distortion and Hilbert transformation in multiply reflected and refracted body waves. *Bull. Seism. Soc. Am.* 65, 1975 (in press)

- Dunkin, J. W.: Computation of modal solutions in layered media at high frequencies. *Bull. Seism. Soc. Am.* 55, 335–358, 1965
- Dziewonski, A. M., Gilbert, F.: Solidity of the inner core of the earth inferred from normal mode observations. *Nature* 234, 465–466, 1971
- Edel, J.-B., Fuchs, K., Gelbke, C., Prodehl, C.: Deep structure of the southern Rhinegraben area from seismic refraction measurements. Submitted to *J. Geophys.*, 1974
- Ewing, W. M., Jardetzky, W. S., Press, F.: *Elastic waves in layered media*. New York: McGraw-Hill Book Comp. 1957
- Fuchs, K.: Das Reflexions- und Transmissionsvermögen eines geschichteten Mediums mit beliebiger Tiefen-Verteilung der elastischen Moduln und der Dichte für schrägen Einfall ebener Wellen. *Z. Geophys.* 34, 389–413, 1968a
- Fuchs, K.: The reflection of spherical waves from transition zones with arbitrary depth-dependent elastic moduli and density. *J. Phys. Earth* 16, Special Issue, 27–41, 1968b
- Fuchs, K., Müller, G.: Computation of synthetic seismograms with the reflectivity method and comparison with observations. *Geophys. J. R. A. S.* 23, 417–433, 1971
- Gilbert, F., Laster, S. J.: Excitation and propagation of pulses on an interface. *Bull. Seism. Soc. Am.* 52, 299–319, 1962
- Haskell, N. A.: The dispersion of surface waves in multi-layered media. *Bull. Seism. Soc. Am.* 43, 17–34, 1953
- HelMBERGER, D. V., Engen, G.: Upper mantle shear structure, *J. Geophys. Res.* 79, 4017–4028, 1974
- Hill, D. P.: An earth-flattening transformation for waves from a point source. *Bull. Seism. Soc. Am.* 62, 1195–1210, 1972
- Hirn, A., Steinmetz, L., Kind, R., Fuchs, K.: Long range profiles in Western Europe: II. Fine structure of the lower lithosphere in France (southern Bretagne). *Z. Geophys.* 39, 363–384, 1973
- Johnson, L. R.: Array measurements of P velocities in the lower mantle. *Bull. Seism. Soc. Am.* 59, 973–1008, 1969
- Kind, R.: Long range propagation of seismic energy in the lower lithosphere. *J. Geophys.* 40, 189–202, 1974
- Mitchell, B. J., HelMBERGER, D. V.: Shear velocities at the base of the mantle from observations of S and ScS. *J. Geophys. Res.* 78, 6009–6020, 1973
- Müller, G.: Theoretical seismograms for some types of point-sources in layered media. Part III: Single force and dipole sources of arbitrary orientation. *Z. Geophys.* 35, 347–371, 1969
- Müller, G.: Approximate treatment of body waves in media with spherical symmetry. *Geophys. J. R. A. S.* 23, 435–449, 1971
- Müller, G.: Amplitude studies of core phases. *J. Geophys. Res.* 78, 3469–3490, 1973a
- Müller, G.: Theoretical body wave seismograms for media with spherical symmetry—discussion and comparison of approximate methods. *Z. Geophys.* 39, 229–246, 1973b
- Press, F.: The earth's interior as inferred from a family of models. In: *The nature of the solid earth* (E. C. Robertson, ed.), 147–171. New York: McGraw-Hill Book Comp. 1972
- Qamar, A.: Revised velocities in the earth's core. *Bull. Seism. Soc. Am.* 63, 1073–1105, 1973
- Roever, W. L., Vining, T. F., Strick, E.: Propagation of elastic wave motion from an impulse source along a fluid-solid interface, I, II, III. *Phil. Trans. Roy. Soc. London, Ser. A*, 251, 455–523, 1959
- Wiggins, R. A., McMechan, G. A., Toksöz, M. N.: Range of earth structure nonuniqueness implied by body wave observations. *Rev. Geophys. Space Phys.* 11, 87–113, 1973

Rainer Kind  
 Gerhard Müller  
 Geophysical Institute  
 University of Karlsruhe  
 D-7500 Karlsruhe  
 Federal Republic of Germany